Operando XRD and electrogravimetry coupling to analyze species transfers during redox processes in Ni/Fe-layered double hydroxide

Elise Duquesne, Stéphanie Betelu, Alain Seron, Damien Bricault, Michel Goldmann, Ioannis Ignatiadis, Denis Limagne, Alina Vlad, Andrea Resta, Hubert Perrot, et al.

Operando XRD and electrogravimetry coupling to analyze species transfers during redox processes in Ni/Fe-layered double hydroxide

Elise Duquesne[a,b], Stéphanie Betelu[b*], Alain Seron[b], Damien Bricault[a], Michel Goldmann[c], Ioannis Ignatiadis[b], Denis Limagne[c], Alina Vlad[d], Andrea Resta[d], Hubert Perrot[a], Ozlem Sel[a] and Catherine Debiemme-Chouvy[a*]

a) Sorbonne Université, CNRS, Laboratoire Interfaces et Systèmes Electrochimiques, UMR 8235, LISE, 4 place Jussieu, F-75005 Paris, France

b) Bureau de Recherches Géologiques et Minières, 3 Avenue Claude Guillemin, F-45100 Orléans, France

c) Institut des NanoSciences de Paris, Sorbonne Université, CNRS, INSP, 4 place Jussieu, F-75005 Paris, France

d) Synchrotron SOLEIL, L'Orme des Merisiers, Saint-Aubin BP48, F-91192 Gif-Sur-Yvette, France

Keywords

Layered double hydroxide (LDH), GIAXRD, ion transfer, EQCM, *ac*-electrogravimetry, OER catalysis

Abstract

A new approach was developed by coupling electrochemical quartz crystal microbalance (EQCM) and Grazing Incidence Angle X-ray Diffraction (GIAXRD) to measure *operando* the current, mass variation and basal spacing of Ni/Fe layered double hydroxide (LDH) under cyclic electrochemical polarization (CEP). It aimed at specifying the redox reactions as well as the ionic and water molecule transfers occurring at the thin LDH film/LiOH aqueous electrolyte interface during the transitional regime and at stationary state. For a better insight, *ac*-electrogravimetry was performed to identify the nature, in terms of the molar mass, the kinetics and the concentration variation of the reversibly transferred species associated with the redox reactions. Ni/Fe-LDH structure is conserved in 1 M LiOH at open circuit potential and during CEPs. In the absence of polarization, CO_3^{2-} anions remain the predominant species into the LDH interlayered spaces. Under polarization, Ni(II) oxidation and Ni(III) reduction occur within the brucite-like layers of the LDH material as well as the oxygen evolution reaction. During the 50 first CEPs, irreversibly oxidized Ni(III) clusters enhance Ni/Fe-LDH conductivity and reversible Ni(III)/Ni(II) redox reaction control anion exchange capacity. OH^- anions become the predominant species into the interlayered spaces and are the unique exchanged anionic species during the faradic process. From the 50th cycle onwards, current, mass variation and basal distance of the electroactivated material oscillate around a stationary value in function of the applied potential, in agreement with the reversible transfer of Li^+, H_2O and OH^-, at different kinetics and concentrations.

1. Introduction

Layered double hydroxides (LDHs) are lamellar inorganic solids constituted of stacked brucite-like layers. They are represented by the general formula: $[M^{(II)}_{1-x}M^{(III)}_{x}(OH)_2]^{x+}(A^{n-}_{x/n}).mH_2O$, where $M^{(II)}$ (*e.g.* Mg^{2+},Co^{2+}, Ni^{2+}...) and $M^{(III)}$ (*e.g.* Fe^{3+}, Al^{3+}, Ni^{3+}…) are the divalent and trivalent cations, respectively, *x* is the mole fraction of $M^{(III)}$ in the total molar quantity of metallic cations. According to the above-mentioned formula, *m* represents the number of inserted water molecules into the interlayer spaces of the LDH structure. In this type of structure, the partial substitution of divalent $M^{(II)}$ by trivalent $M^{(III)}$ metallic cations results in an excess of positive charges in the octahedral layers. This excess of positive charges is compensated by the presence of exchangeable hydrated anions in the interlayer space of the solid.[1] This leads to provide LDHs a high capacity for anion exchange (2-4 $meq \cdot g^{-1}$).[2,3,4]

The LDHs bearing electroactive metal cations within their structure could undergo reversible electrochemical reactions[1,5,6,7,8] accompanied with the transfer of anions. As an example, in Ni/Fe-LDH, known to be one of the most conductive LDHs, electroactive Ni can be switched in oxidation states during cyclic voltammetry in NaOH (0.1 M)[6], following:

$$\text{LDH-Ni(II)} + OH^- \leftrightarrows \text{LDH}(OH^-)\text{-Ni(III)} + e^- \quad (1)$$

By *in situ* XRD study on Ni/Fe-LDHs under cyclic electrochemical polarization (CEP) and *ac*-electrogravimetry measurements conducted during the stationary state, Duquesne *et al.*[9] demonstrated reversible OH^- intercalation into the interlayer space during Ni(II) oxidation and, OH^- deintercalation from the interlayer space during Ni(III) reduction in 1 M KOH ; both phenomena are accompanied by a simultaneous and reversible counterflux of water molecules from/into the Ni/Fe-LDHs interlayered space. This expulsion/insertion of water molecules is related to the modulation of the Coulombian interactions between layers and interlayered OH^-, during Ni oxidation/reduction reactions.

In addition, the adsorption/desorption of cations onto/from LDH sheets also occurs under CEP in alkaline solution, in which the reactivity of external surfaces is strongly influenced by the net proton surface charge, which depends on the electrolyte pH, with respect to the Brønsted–Lowry acid-base theory, through the following reaction:

$$\equiv M\text{-}OH \leftrightarrows \equiv M\text{-}O^- + H^+ \quad (2)$$

where M is a metallic cation constituting the layered sheets. For pH >> pH_{PZNC} (pH of zero point of net charge (ZPNC)), $\equiv M\text{-}O^-$ group predominate, leading to cation sorption.

For example, it has been observed that a reversible Na^+ adsorption onto Mg/Fe-LDH sheets occurs under CEP in sodium carbonate buffer solution.[10] In the same way, Duquesne *et al.*[9] have demonstrated K^+ adsorption/desorption phenomena in 1 M KOH electrolyte during CEP using Ni/Fe-LDH, in agreement with the following reaction:

$$\equiv M\text{-}O^- + K^+ \leftrightarrows \equiv M\text{-}O\ K \qquad (3)$$

Actually, under CEP in an alkaline solution, oxygen evolution reaction (OER) induces a decrease of the interfacial pH that is approaching the pH_{PZNC} of the Ni/Fe-LDHs whose value is 8. This leads to re-protonation of the surface hydroxyl groups and electrolytic cation desorption (**Eq. 3**). This finding has confirmed the LDH electroadsorption properties with mix cation and anion exchanges.

In this article, we specified concomitantly the structural behavior of Ni/Fe LDH, the electrochemical response of Ni^{III}/Ni^{II} redox active cations constituting the lamellar sheets as well as the mass transfers into/from the solid during the whole electrochemical process*, i.e.* during both the transitional regime and at stationary state. To this aim, a novel *operando* approach was developed and implemented at Synchrotron Soleil. The coupling of Grazing Incidence Angle X-ray Diffraction (GIAXRD) and electrochemical quartz crystal microbalance (EQCM) measurements was possible due to the design of an original homemade imprinted electrochemical cell. This allowed us to investigate further the charge compensation mechanisms of a Ni/Fe-LDH thin film immersed in LiOH electrolyte during Ni oxidation/reduction reactions and OER. Indeed, since the 2010s, the synthesis of Ni-based LDHs and their derivate has been extensively investigated for the development of efficient, reliable and robust catalysts or supercapacitors.[11,12,13,14,15] The control of the electrochemical properties as well as the correlations between electrochemical properties and structure are of prime interest to envisage breakthrough electrolysis processes for the selective or the universal capture and release of ions in various/several fields such as energy storage but also of water treatment and industrial effluent treatment.

To this aim, an *operando* approach was developed and implemented consisting in applying CEP and monitoring simultaneously (i) current, (ii) LDH interlamellar space and (iii) electrode mass variation during redox reactions associated to ion and water molecule transfers. This approach required the coupling between GIAXRD using a synchrotron source and EQCM measurements. This paves the way towards new *in situ* tools for the characterization of the transfer mechanisms of species during the whole life cycle of crystalline materials, from transitional regime and stationary regime to end of life cycle.

Besides *operando* XRD/EQCM studies, we performed an in-depth investigation of the (electro)adsorption of electrolytic alkali cations during LDH electrode polarization by *ac*-electrogravimetry measurements. The latter couples electrochemical impedance spectroscopy and fast quartz crystal microbalance measurements performed under an applied potential, in order to determine the species (anion, cation, solvent molecule) which are transferred and their transfer kinetic parameters and concentration variation.

2. Experimental part

All chemicals (Normapur, more than 99.8% of purity) used for the Ni/Fe-LDH synthesis and the electrolyte salt were supplied by Merck-Sigma-Aldrich (Merck KGaA, Darmstadt, Germany): $Ni(NO_3)_2.6H_2O$, $Fe(NO_3).9H_2O$, Na_2CO_3, $NaHCO_3$ and LiOH.

2.1. LDH synthesis by co-precipitation and preparation of a coated electrode

The Ni^{II}/Fe^{III}-CO_3-LDH 6/2 (LDH with Ni/Fe atomic ratio equals to 6/2 and carbonate anions in the interlayer space) was chemically synthesized using the varying pH method under air at 35°C.[16] $Ni(NO_3)_2.6H_2O$ and $Fe(NO_3)_3.9H_2O$ salts were dissolved in deionized water (Milli Q 18 MΩ) at a concentration of 0.15 M and 0.05 M, respectively, leading to a solution with a Ni^{II}/Fe^{III} molar ratio equal to 3. The metallic cations (Ni^{2+} and Fe^{3+}) were co-precipitated by an alkaline aqueous solution containing 1 M Na_2CO_3 and 2.6 M NaOH, introduced drop-wise at a constant rate by means of a peristaltic pump until the solution reached a pH value of 10 under vigorous stirring. The slurry was then stirred during 24 h at 60°C for maturation, in order to make LDH particles growing and their crystallinity enhanced. To eliminate the supernatant, the slurry was centrifuged at 4000 rpm during 5 minutes. Finally the material underwent five dialyses in carbonate solution and then deionized water to allow nitrate to carbonate exchange and suppress salt excess. A photo of the slurry is shown in **Figure S1-A**. After drying, the LDH powder was characterized by XRD and SEM observations (**Figure 1A** and **S1**). The XRD pattern of the Ni/Fe-LDH is shown in **Figure 1-Ab**. The diffraction peaks at 2θ of 11.6°, 23.2°, 34.5°, 39.1°, 46.5°, 59.9°, and 60.9° could be assigned to the (003), (006), (012), (015), (018), (110) and (113) plane reflections, respectively (ICDD card Nº 01-082-8040; **Figure S1-C**). SEM micrographs of the LDH nanoplatelets are presented in the inset of **Figure 1** and in **Figure S1-B**. Further characterizations (EDX, XPS) of the Ni/Fe LDH are presented in Ref. 9 in which the same LDH material was studied.

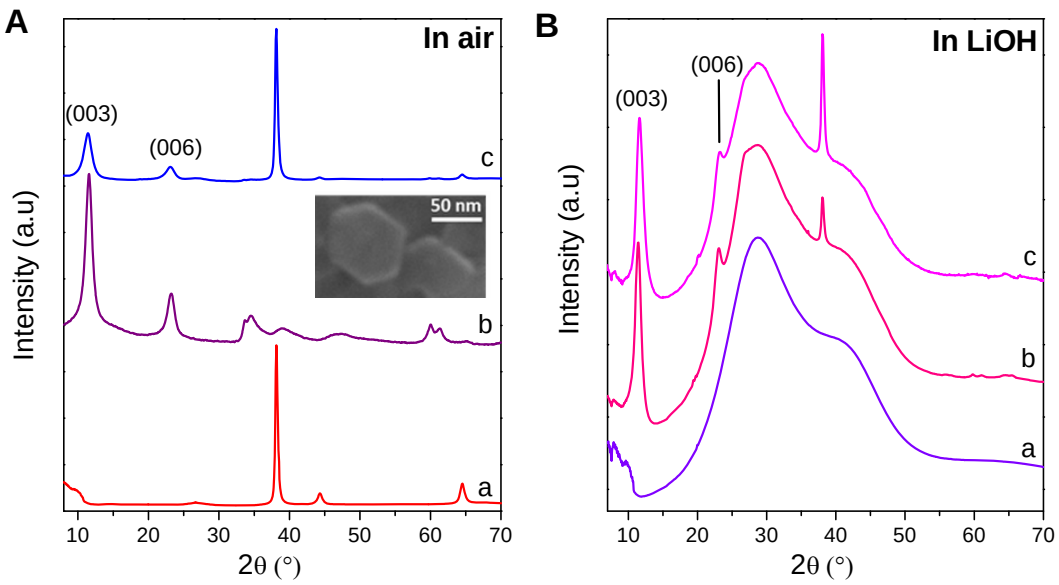

***Figure 1**: XRD patterns A) in air of a) Au/quartz, b) powder of Ni^{II}/Fe^{III}-CO_3-LDH 6/2, c) Au/quartz coated with Ni^{II}/Fe^{III}-CO_3-LDH 6/2 ; B) in LiOH 1 M of a) electrolyte, b) and c) Au/quartz coated with Ni/Fe-LDH before and after electrochemical experiment, respectively. Insert: SEM micrograph of nanoplatelets of Ni/Fe-LDH.*

For the preparation of the electrodes, the slurry was prepared by dispersing the Ni/Fe-LDH powder in ethanol and deposited on gold-patterned quartz resonator substrates (9 MHz-AWS, Valencia, Spain). The deposition of Ni/Fe-LDH film was carried out according to the drop casting method described in the literature[17,18] onto the gold surface (surface area: 0.20 cm^2) of the gold-patterned quartz substrates. 10 µL of the Ni/Fe-LDH suspension were deposited and then, dried in air for a few hours. The XRD pattern obtained for the Au/quartz coated with Ni/Fe-LDH is shown in **Figure 1-Ac**. The main diffraction peaks of the Ni/Fe-LDH at 2θ of 11,6 and 23,2° are detected. The thickness of the dried Ni/Fe-LDH film was estimated to be around 500 nm (based on FEG-SEM measurements)[9].

2.2 EQCM coupled to *operando* XRD measurements

A home-made 3D-imprinted electrochemical cell (**Figure 2**) was designed and developed to simultaneously record both EQCM data and XRD pattern of the Ni/Fe-LDH working electrode immersed in an aqueous solution of 1 M LiOH.

EQCM measurements were performed using a three-electrode system connected to an Autolab potentiostat/galvanostat electrochemical workstation coupled with a lab-made QCM device. All the potentials of the saturated calomel reference electrode (SCE) were converted to the standard hydrogen electrode (SHE). The counter-electrode was a platinum grid, the working electrode

(WE) was a 9 MHz-gold patterned quartz substrate coated with a thin film of Ni/Fe-LDH. Frequency changes (Δf) of the quartz crystal resonator were simultaneously monitored with the current response. The Δf response was converted into the mass change (Δm) by applying the Sauerbrey equation[19] (**Eq. 4**):

$$\Delta f = \frac{2f_o^2}{A\sqrt{\rho_q \mu_q}} \Delta m = -C_f \, \Delta m \quad (4)$$

where A is the active surface of the gravimetric sensor, ρ_q is the quartz density, μ_q is the quartz shear modulus, f_0 is the fundamental resonance frequency of the quartz and C_f is the experimental sensitivity constant equals to 16.31×10^7 Hz.g^{-1} cm^2 for 9 MHz.[20]

The electrochemical cell with Kapton windows 30 µm thick was installed on the SIXS beamline at the synchrotron SOLEIL for GIAXRD measurements. The energy of the incident beam was set at 20 keV (λ = 0.062 nm) allowing at transmission of about 20% through 2 cm of electrolyte.

The spot size 1000 × 50 µm^2 (horizontally × vertically) reached the quartz surface at a grazing incidence of 0.05 radian and the diffracted beam was recorded by a 2D XPad detector in Q-range between 0.5 Å^{-1} and 1.1 Å^{-1}. We focus on the 003 Bragg reflection which was recorded at each second and fitted by a Lorentzian function to determine the intensity and position of the peak (versus polarization time, *i.e.* applied potential).

During CEP, three parameters were simultaneously recorded: (i) the current at the Ni/Fe-LDH working electrode, (ii) the microbalance frequency of the quartz resonator coated with the Ni/Fe-LDH film and (iii) the characteristics of the (003) Bragg diffraction peak of the Ni/Fe-LDH pattern. The latter was fitted with a Lorentzian curve to obtain Q, the scattering vector of the peak, which gives the basal distance d following **Eq. 5**:

$$Q = \frac{4\pi}{\lambda} \, sin\,(\theta) = \frac{2\pi}{d} \quad (5)$$

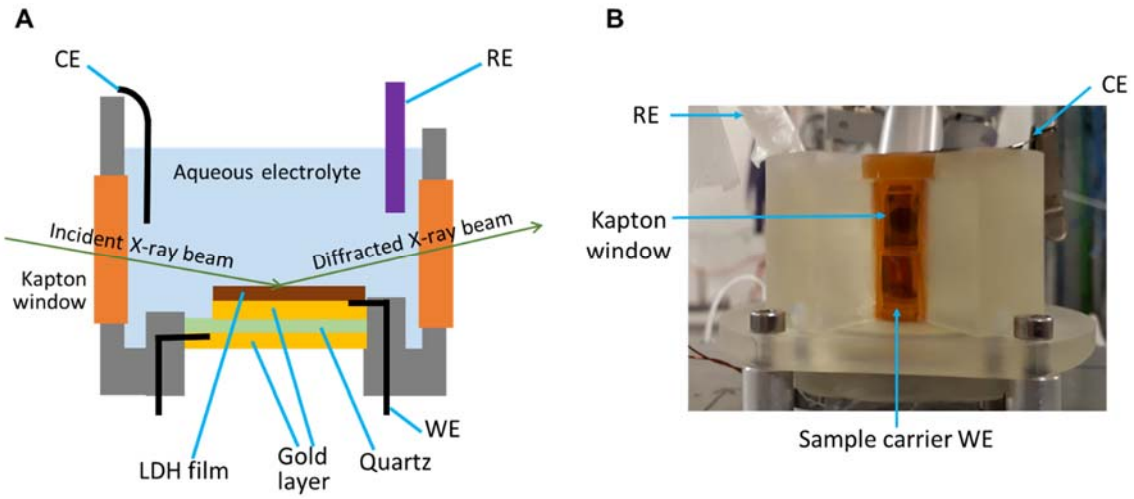

Figure 2: *(A) Schematic and (B) experimental setup of the home-made 3D-imprinted electrochemical cell used at synchrotron SOLEIL SIXS beamline for operando XRD and electrogravimetry coupling. WE: working electrode (Ni/Fe-LDH film deposited on Au-coated quartz resonator). CE: counter electrode. RE: reference electrode.*

2.3 *Ac*-electrogravimetry

The *ac*-electrogravimetric setup was composed of a four-channel frequency response analyzer (FRA, Solartron 1254) coupled to a lab-made potentiostat (SOTELEM-PGSTAT) and a lab-made QCM operating under dynamic regime.[21, 22] The Ni/Fe-LDH electrode was polarized at a given potential, to which a sinusoidal small amplitude potential perturbation (80 mV rms) was superimposed. The microbalance frequency change (Δf) related to the mass response (Δm) of the Ni/Fe-LDH-coated gold electrode was measured simultaneously with the current response (ΔI) of the electrochemical system. The resulting signals were sent to the four-channel FRA at a given potential and frequency modulation to obtain two main experimental transfer functions (TFs) (i) electrogravimetric TF, $\frac{\Delta m}{\Delta E}|_{exp}(\omega)$, and (ii) classical electrochemical impedance, $\frac{\Delta I}{\Delta E}|_{exp}(\omega)$. The latter permits the experimental charge/potential TF, $\frac{\Delta q}{\Delta E}|_{exp}(\omega)$, to be obtained, according to the following equation:

$$\frac{\Delta q}{\Delta E}|_{exp}(\omega) = \frac{1}{j\omega}\frac{\Delta I}{\Delta E}|_{exp}(\omega) \quad (6)$$

From the experimental electrogravimetric TF, $\frac{\Delta m}{\Delta E}|_{exp}(\omega)$, experimental partial TFs can be calculated, eliminating the contribution of an anion or a cation, if three species are taken into

account: a cation (c), an anion (a) and free solvent molecule (s) (see **Figure S2**). For example, if the contribution of the cation is extracted, the remaining experimental response of the anion and the solvent is calculated according to the following equation:

$$\frac{\Delta m}{\Delta E}\Big|_{exp}^{as}(\omega) = \frac{\Delta m}{\Delta E}\Big|_{exp}(\omega) + \frac{m_c}{F}\frac{\Delta q}{\Delta E}\Big|_{exp}(\omega) \quad (7)$$

In a similar manner, if the contribution of the anion is extracted, it becomes:

$$\frac{\Delta m}{\Delta E}\Big|_{exp}^{cs}(\omega) = \frac{\Delta m}{\Delta E}\Big|_{exp}(\omega) - \frac{m_a}{F}\frac{\Delta q}{\Delta E}\Big|_{exp}(\omega) \quad (8)$$

Experimental TFs were fitted with the theoretical expressions defined in a model based on the interfacial flux of species under polarization (**Eq. 9** and **10**) using Mathcad Software version 15 (PTC).

$$\frac{\Delta q}{\Delta E}(\omega)\Big|_{th} = F d_f \sum_i = \frac{G_i}{j\omega d_f + K_i}(\omega) \quad \text{(i: cation, anion)} \quad (9)$$

$$\frac{\Delta m}{\Delta E}(\omega)\Big|_{th} = -d_f \sum_i M_i \frac{G_i}{j\omega d_f + K_i}(\omega) \quad \text{(i: cation, anion, solvent molecule)} \quad (10)$$

where G_i (= $1/Rt_i$) describes the ease or difficulty of interfacial transfer for each species transferred at the electrode/electrolyte interface, K_i represents the kinetics rate of transfer, ω is the pulsation, d_f is the film thickness, F is the Faraday constant, and M_i is the molar mass of the involved species. Therefore, fitting procedure provided parameters (K_i, G_i, M_i and C_i-C_0 (**Eq. 11**)) regarding the nature of the species transferred, together with their interfacial dynamics and their concentration variation inside the electrode material.

$$\frac{\Delta C_i}{\Delta E}(\omega) = \frac{-G_i}{j\omega d_f + K_i} \quad (11)$$

3. Results and discussion

3.1 *Operando* XRD coupled to EQCM measurements

The structure of Ni/Fe-LDH was firstly investigated by XRD in 1 M LiOH in the absence of any polarization and under CEP by EQCM measurements. Figure 1-B shows XRD patterns recorded in LiOH solution: only the solution (pattern a), LDH coating (patterns b and c). The

(003) and (006) diffraction peaks due to the LDH are still well detected in LiOH solution.

3.1.1 *Operando* XRD in the absence of polarization

Figure 3A shows the Q_{003}-peak position of a thin Ni/Fe-LDH coating immersed in 1 M LiOH without any polarization. Under this condition, the peak position, intensity and full width at half maximum (FWHM) remained constant over the immersion time (2900 sec). In comparison with the value of basal spacing of 7.55 Å ($Q = 0.832$ Å^{-1}) for OH-based interlayered 6/2 $M^{(II)}/M^{(III)}$ ratio-based LDHs[23], herein the basal spacing is 7.77 Å ($Q = 0.809$ Å^{-1}, **Figure 3A**), in agreement with the predominance of CO_3^{2-} in the interlayer space[24,23,25,26]. Indeed, when CO_3^{2-} is the predominant anion into the interlayer space, the basal spacings provided by Miyata in 1975[26], in 1980[25] and in 1983[23], and by Kameda in 2006[24], are 7.67 Å, 7.80 Å and 7.65 and 7.80 Å, respectively.

LDHs generally exhibit a strong affinity for CO_3^{2-} anions[23]. Although the choice of metallic element M and $M^{(II)}/M^{(III)}$ ratio greatly influence the nature and the content of interlayer anions, 6/2-based LDHs have relatively weak affinity for monovalent anions.[23, 27, 28] Moreover, the comparison of the ion-exchange equilibrium chemical constants of 6/2-based LDHs[23] with respect to CO_3^{2-} ($\log K = 1.84$ using Gaines-Thomas expression[29]*)* and OH^- ($\log K = 1.42$ using Gaines-Thomas expression[29]) shows that CO_3^{2-} remains the predominant anion into the pristine LDH material (not electrochemically modified).

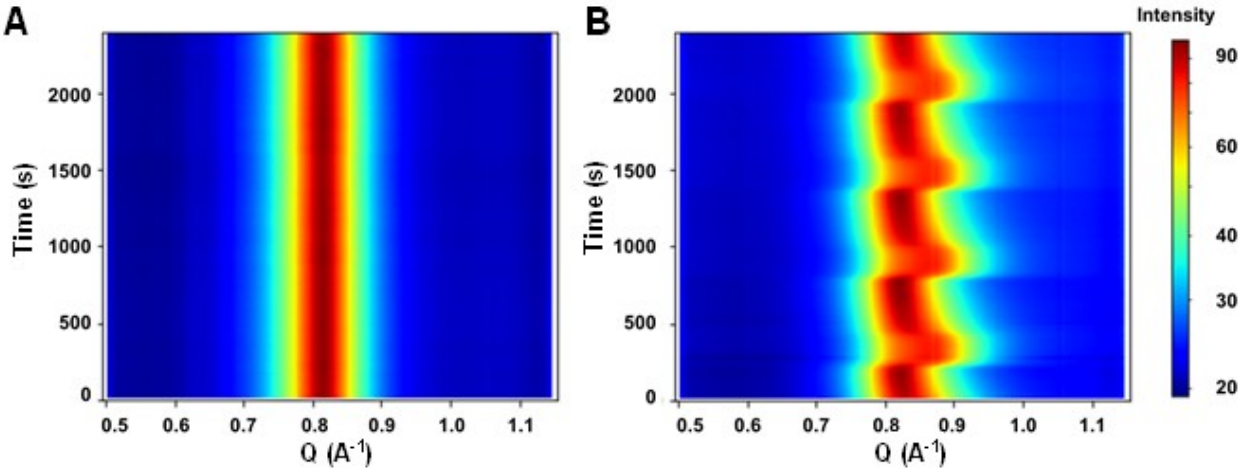

Figure 3*: Evolution of the Q_{003}-peak position of the Ni/Fe-LDH immersed in 1 M LiOH, (A) in the absence of any polarization, (B) under 4 CEPs, between 0.44 V/SHE and 0.73 V/SHE, at a scan rate of 1 mV·s^{-1}.*

3.1.2. *Operando* XRD coupled to EQCM under cyclic polarization

3.1.2.1. Investigations at 10 mV·s^{-1}

After having remained at open circuit potential for 2900 s, the Ni/Fe-LDH film underwent 81 CEP, in the range from 0.44 V to 0.73 V *vs.* SHE, at 10 mV·s^{-1}. The current (I), mass variation (Δm) and Q_{003}-peak position of the LDH material were simultaneously recorded as a function of time, until reversibility of these parameters was observed (**Figure 4**), *i.e.* the current, the basal spacing and the mass oscillated around the same value from one cycle to another. As shown in **Figure 4**, this was the case after the 50th CEP. The 50 first cycles correspond to an activation process of the LDH material. **Figure S3A** shows the peak current densities at each cycle, one anodic due to Ni(II) oxidation and one cathodic due Ni(III) reduction; it also shows the current density of the anodic limit due to OER. **Figure S3B** presents the ratio between the anodic and the cathodic peak current densities of the Ni(II) oxidation and the Ni(III) reduction, respectively. After 5 cycles, the ratio value is lower than -1, this could indicate that the current density due to Ni(II) oxidation is always higher than the current density due to Ni(III) reduction. After 16 CEP this ratio reaches a value lower than -2, showing an increase in some irreversibly Ni(III) clusters enhancing the conductivity of the Ni/Fe-LDH. Moreover after 50 cycles, the currents at 0.690 and 0.575 V/SHE are constant (**Figure S3A**), indicating that the Ni(II) and Ni(III) contents do not vary anymore. Since the ratio is lower than -1, it equals to -1.8, one can conclude that OER occurs at this potential (0.69 V/SHE).

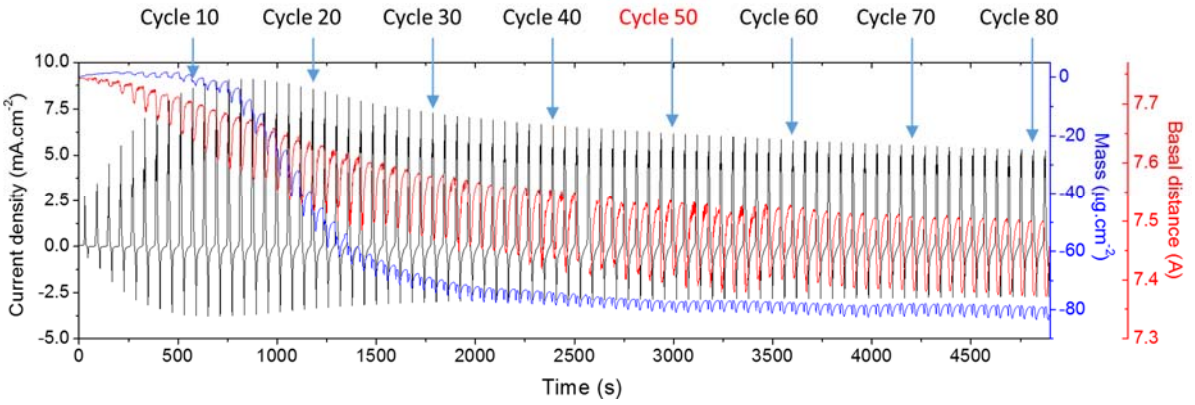

Figure 4. *Operando coupled EQCM/XRD measurements obtained from a thin film of Ni/Fe-LDH immersed in 1 M LiOH under cyclic polarization at 10 mV·s^{-1}, between 0.44 V/SHE and 0.73 V/SHE. Variation of current density (in black), mass variation (in blue) and basal spacing (in red) during 81 polarization cycles.*

During the ten first cycles, the maximum current density J, of Ni(II) oxidation peak increased versus incremented cycles (**Figure 4**, black line and **Figure S3**). The maximum current of the Ni(III) reduction peak also increased, but always with a lower absolute value (**Figure S3B**). Although, the current density of Ni(II) oxidation is concomitant with OER, this finding is in good agreement with the increase in some irreversibly oxidized Ni(III) clusters that enhance the conductivity of the Ni/Fe-LDH[9,30,31,32,33,34]. Simultaneously, without taking into account the oscillations within each electrochemical cycle (that will be discussed thereafter), the global mass remained nearly stable (**Figure 4**, blue line) whereas the basal spacing, *d*, began to decrease (**Figure 4**, red line).

From cycle number 15 to 22, both mass and basal spacing linearly decreased (**Figure 4**, blue line and red line, respectively). From CEP number 22 to cycle 50, these parameters decreased to a lesser extent, From CEP cycle number 50, the electroactive material presented a reproducible and reversible electrogravimetric and crystallographic behavior; *i.e.* from one cycle to another at a given potential, the recorded parameters remained the same.

The variations of the electrode mass and decrease in *d versus* the applied potential are in agreement with the progressive substitution of one CO_3^{2-} anion (60 $g \cdot mol^{-1}$) by 2 OH^- anions (34 $g \cdot mol^{-1}$) into the interlayer space. From cycle number 50, the basal spacing oscillated between 7.38 Å and 7.50 Å, in agreement with the predominance of OH^- anions in the interlayer space[23]: no more residual CO_3^{2-} are exchanged into the interlayer space.

Under polarization, *J*, Δm and *d* oscillate around a stationary value in function of the applied potential (starting from the 50th cycle). To accurately analyze the data, the potential scan rate was decreased to 1 $mV \cdot s^{-1}$ in the next section.

3.1.2.2. Investigations at 1 $mV \cdot s^{-1}$, after the activation process

After the 81 CEP, the potential scan was decreased to 1 $mV \cdot s^{-1}$. **Figure 3B** shows the 003-peak position variation under CEPs and **Figure 5** shows the electrogravimetric behavior as well as the basal spacing evolution of the LDH material under only one polarization cycle. The basal spacing oscillates between 7.38 Å and 7.5 Å. This finding comforts the data acquired at 10 $mV \cdot s^{-1}$: OH^- anions are the prevalent species transferred into the interlayer space.

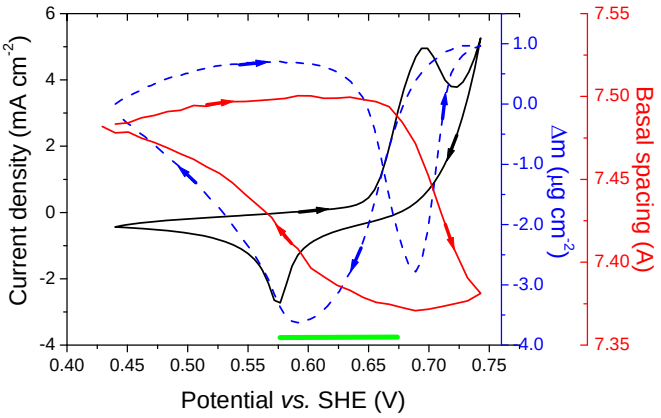

Figure 5: *Operando coupled XRD and EQCM measurements obtained from thin film of Ni/Fe-LDH immersed in 1 M LiOH under cyclic polarization at 1 mV·s^{-1}. Current density (in black), mass variation (in blue) and interlayered spacing variation (in red) vs. applied potential. Green line: potential domain studied by ac-electrogravimetry.*

In **Figure 5**, the current *vs.* potential curve (black line) clearly shows a broad anodic peak (at 0.69 V *vs*. SHE) due to the concomitant Ni(II) oxidation and OER and, a cathodic peak (at 0.575 V *vs*. SHE) in agreement with the reduction of Ni(III) sites into the brucite-like layer of the LDH material. The peak separation (115 mV) denotes a slow charge transfer in agreement with bibliography.[6,9]

From the observation of the gravimetric response (dashed blue line, **Figure 5**), during the anodic sweep, as soon as the anodic current density appeared (0.63 V *vs.* SHE) the Ni/Fe-LDH film underwent first a mass depletion until 0.68 V. Then, the mass increased and finally reached a plateau at 0.72 V. The basal spacing (red line, **Figure 5**) remains constant until 0.66 V then it progressively decreased.

Actually, during the anodic sweep, the modification in the redox state of Ni(II) to Ni(III) could conduct to three phenomena appearing almost concomitantly[9]:

(i) An increase in Coulombic interactions between intercalated OH^- anions and more positively charged adjacent layers, resulting in a decrease in basal spacing (red line, **Figure 5**) and mass increase.

(ii) H_2O molecule de-intercalation leading to a decrease in basal spacing and to the LDH material mass.

(iii) Li^+ desorption from the external LDH sheets leading to the electrode mass decrease.

The OH^- intercalation is clearly shown by QCM when the Ni(II) oxidation current reached 3/4 of the peak current. Regarding the LDH structure by *operando* XRD, the electroactive attraction between the anions and the positively charged layer is the prevailing phenomenon from the 3/4 of the Ni(II) oxidizing process. As EQCM provides an overview of the global mass change, multi-species contribution in the charge compensation process is not easily distinguishable. Therefore, the lithium contribution cannot be assessed by classical electrogravimetry (this be discussed thereafter).

During the reverse scan (from 0.73 V to 0.44 V *vs.* SHE), a mass decrease was observed until a cathodic current due to Ni(III) reduction appears leading to a mass increase. As soon as the cathodic current appeared the basal spacing increased to its initial value.

The modification in the redox state of Ni(III) to Ni(II) also implied different phenomena with different kinetics:

(i) The OH^- deintercalation in the potential range at which the cathodic current nearly reached its maximum (0.57 V/SHE),
(ii) The electrostatic repulsion between the adjacent LDH layers leading to d increase
(iii) H_2O re-intercalation leading to the increase of the basal distance and of the electrode mass
(iv) Li^+ electroadsorption

In agreement with literature[9], as previously mentioned, Li^+ could also be involved in the charge compensation process and the mass change during the electrochemical reactions. As EQCM provides an overview of the global mass change, multi-species contribution in the charge compensation process is not easily distinguishable. For this reason, *ac*-electrogravimetric experiments were conducted to specify the nature of the species transferred during Ni oxidation/reduction. It leads to a better insight into the mechanisms of species transfer as well as the determination of the kinetics constants and the concentration variation of the involved species.

3.2 *Ac*-electrogravimetry

Ac-electrogravimetric experiments were performed to gain insight into: (i) the identification of the nature (cation, anion or water molecule) and molar mass of each transferred species, (ii) the kinetics of each charged and uncharged species transfer at the LDH/electrolyte interface, and

(iii) the evaluation of their respective concentration variations and kinetics as a function of the applied potential. *Ac*-electrogravimetry was carried out in 1 M LiOH using a new LDH electrode, after 50 potential cycles from 0.44 V/SHE and 0.73 V/SHE at 10 $mV \cdot s^{-1}$ in order to have a stabilized LDH film (based on the profiles shown in **Figure 4**).

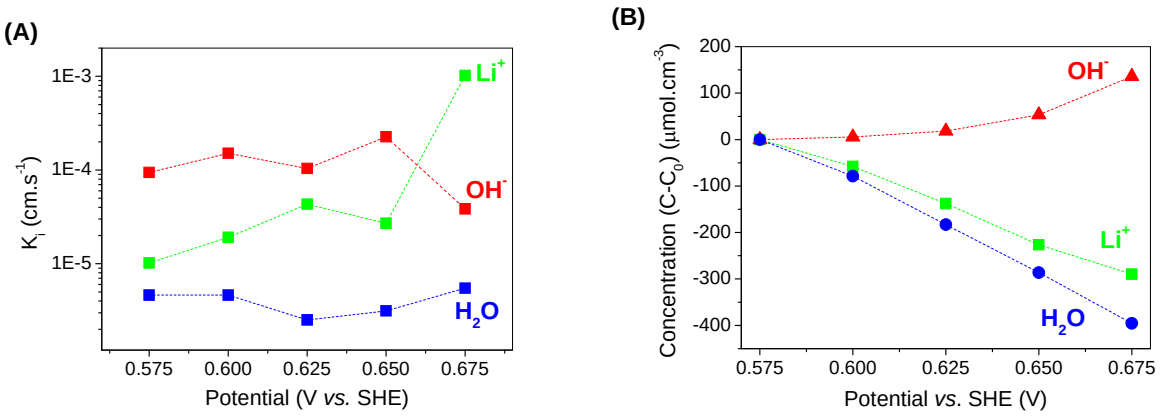

Figure 6: *Ac-electrogravimetric results. (A) Kinetics parameters K_i of Li^+, OH^- and H_2O vs. the applied potential of Ni/Fe-LDH. (B) Relative concentration variations, Ci–C_0, of Li^+, OH^- and H_2O transferred to the Ni/Fe LDH-coated Au electrode vs. the applied potential. Electrolyte: 1 M LiOH.*

The fitting of the experimental data (see **Figure S3**) shows that three species are involved, *i.e.* OH^-, Li^+ and water molecule, during the redox processes. **Figure 6A** and **S2b** show that at high frequencies OH^- ions are exchanged, at intermediate frequencies Li^+ ions are implied (excepted at 0.675 V *vs*. SHE) whereas at low frequencies free water molecules are involved. This result was confirmed by calculated partial TFs (**Eq. 7** and **8, Figure S2c** and **S2d**). **Figure 6B** represents the evolution of the relative concentration change of each species (**Eq. 11**) in the potential range indicated in **Figure 5**. It shows that when the Ni/Fe-LDH material is oxidized, Li^+ ions and H_2O molecules are transferred from the LDH to the electrolyte whereas OH^- ions have an opposite flux direction so that they are transferred from the electrolyte to the LDH material. The inverse processes take place during reduction of Ni(III).

According to **Figure 6B**, the concentration of deintercalated H_2O molecules is about three times higher than that of intercalated OH^-, leading to **Eq. 12**:

$$[Ni^{II}_6Fe^{III}_2(OH)_{14}(OH)_2],yH_2O + xOH^- \leftrightarrows [Ni^{II}_{6-x}Ni^{III}_xFe^{III}_2(OH)_{14}(OH)_{2+x},(y-3x)\ H_2O + 3xH_2O + xe^- \quad (12)$$

This, together with the (electro)desorption of Li^+, explains the global mass loss observed by EQCM in the range 0.625 V to 0.675 V *vs*. SHE when the applied potential is increased; the water deintercalation is the dominant phenomenon.

The global mass gain noticed in the range 0.700 V to 0.740 V *vs.* SHE by EQCM (**Figure 5**, dashed blue line) was not investigated by *ac*-electrogravimetry due to high irreversible OER reaction. Here, the only way to explain the mass gain is the domination of OH^- intercalation in terms of mass compared to the deintercalation of water molecules and desorption of Li^+.

Concomitantly, Li^+ desorption from the LDH sheet surface can be related to the variation of the pH at the LDH/electrolyte interface *via* the catalyzed OER[10] (**Eq. 13**):

$$[Ni^{II}_6Fe^{III}_2(OH)_{14-w}(OLi)_w(OH)_2],yH_2O + (2z-w)OH^- \leftrightarrows [Ni^{II}_6Fe^{III}_2(OH)_{14}(OH)_2],yH_2O + (z-w)H_2O + 2ze^- + wLi^+ + zO_2 \quad (13)$$

The charge compensation phenomenon (**Eq. 14**) could also be corroborated by the evolution of the relative concentration of OH^- and Li^+ (**Figure 6B**) at the interface for the lower investigated potentials (below 0.650 V/SHE). Indeed, the OH^- concentration variation remains five times lower than the one of Li^+ whereas OER seems very low (no interfacial pH variation). Moreover, the basal spacing does not vary in such a potential range.

$$[Ni^{II}_6Fe^{III}_2(OH)_{14-w}(OLi)_w(OH)_2],yH_2O \leftrightarrows [Ni^{II}_{6-x}Ni^{III}_xFe^{III}_2(OH)_{14-w}(OLi)_{w-x}(O^-)_x(OH)_2],yH_2O + xe^- + xLi^+ \quad (14)$$

Surface charge compensation involving Li^+ due pH variation at the LDH/electrolyte interface (**Eq. 13**) and to Ni(II) oxidation (**Eq. 14**) can be differentiated by data reported in **Figure 6A** that presents the evolution of the kinetic parameters, K_i, of each species over the potential range 0.575 V to 0.675 V *vs*. SHE. Indeed, the kinetics of Li^+ remains the same in the range from 0.575 to 0.650 V. It drastically increases at 0.675 V from 10^{-5} to 10^{-3} cm s^{-1}. Therefore we assume that at the lower potentials, the Li^+ desorption from external surfaces is due to charge compensation (**Eq. 12)** whereas at the highest potential, it is due to pH variation due to OER (**Eq. 13**).

Based on K_i values, the OH^- ion is the fastest of the three species transferred at each potential from 0.575 V to 0.650 V *vs.* SHE, followed by Li^+ and H_2O. Li^+ becomes the fastest at the highest potential (0.675 V *vs*. SHE). This is in good agreement with its faster desorption as the pH decreases when OER occurs. By comparing the kinetics parameters of OH^- and H_2O, whatever the applied potential K_{OH^-} is superior to K_{H2O}, this could be related to a faster OH^-

intercalation (faradaic process, charge compensation due to Ni(II) oxidation), followed by a subsequent slow release of H_2O even if the concentration of water molecules exchanged is higher (**Figure 6A**).

Previous similar transfer mechanisms were observed in 1 M KOH.[9] Whatever the investigated electrolyte (KOH or LiOH), the electrochemically induced transfers imply a reversible flux of OH^- anions and a counterflux of dehydrated alkali cations (K^+, Li^+) and free H_2O molecules, however presenting different kinetics and relative concentration variations. Moreover, contrary to K^+, Li^+ desorption/sorption from/onto the external surfaces of the LDH nanoplatelets is involved into charge compensation due to Ni oxidation/reduction reactions and OER.

Figure 7 schematizes the processes occurring in/at Ni/Fe-LDH during CEP in 1 M LiOH, after the activation process (50 CEPs) of the LDH (Ni(III) formation and replacement of CO_3^{2-} by OH^- between the LDH sheets).

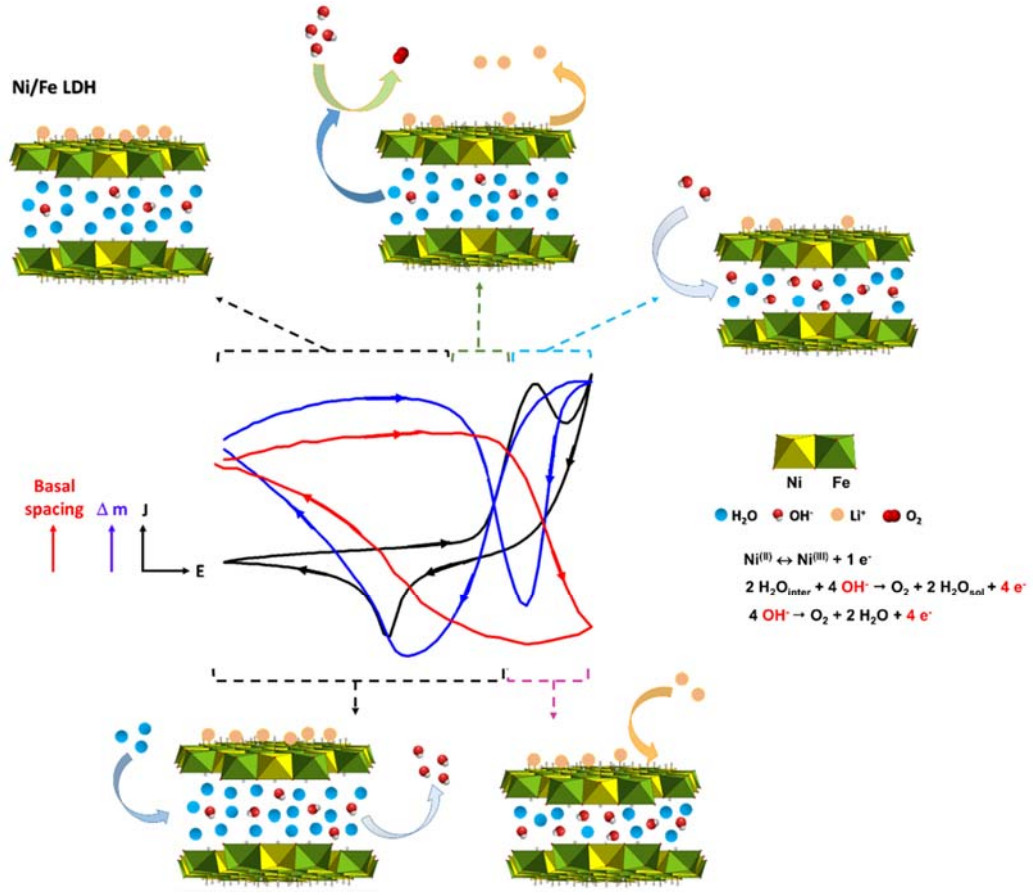

Figure 7: *Schemes showing the various electron and species (ions and water) transfers during Ni/Fe polarization in 1 M LiOH after activation for 50 cycles during which exchange between CO_3^{2-} and OH^- and Ni(III) production occur.*

At the beginning of Ni(II) oxidation, in the range from 0.600 V to 0.650 V *vs.* SHE, the charge transfer is compensated by Li^+ electro-desorption from the LDH external surfaces (**Eq. 14**). Ac-electrogravimetry was used to confirm this contribution because multi-species contribution with different flux directions is rather complex to be detected only by EQCM. From 0.675 V *vs* SHE, the gravimetric behavior suits the assumption of a switch in Ni(III)/Ni(II) redox state that induces OH^- intercalation within the interlayer space in agreement with a counterflux of water molecules due to the shifting of Coulombian forces (**Eq 12**). OH^- is the prevalent anion in the basal spacing which varies between 7.50 Å (at 0.45 V *vs.* SHE) and 7.38 Å (at 0.75 V *vs*. SHE). The basal spacing decrease observed by *operando* XRD is also due to H_2O deintercalation. Concomitantly, the pH variation due to catalyzed OER caused external surface group protonation and thus Li^+ desorption from external surfaces (**Eq 13**).

During the cathodic sweep, Li^+ sorption onto the negatively charged external surface of the LDH nanoplatelets occurs when the OER stops. The OH^- deintercalation is then predominant in the potential range where Ni(III) reduction reaction occurs. Finally, at lower potentials, interlayer hydration is the predominant phenomenon as deducted from EQCM and XRD results.

4. Conclusions

In addition to *ac*-electrogravimetry, the coupling of *operando* EQCM and GIWAXS allowed redox reactions as well as the corresponding mass transfer mechanisms and structural behavior occurring at Ni/Fe LDH thin film, in LiOH aqueous solution (1 M) to be deeply examined.

In the absence of polarization, CO_3^{2-} anions remain the predominant species into the interlayered space. Under polarization, the current *versus* potential curve clearly shows a broad anodic peak (at 0.69 V *vs*. SHE) due to the concomitant Ni(II) oxidation and OER and a broad cathodic peak (at 0.575 V *vs*. SHE) in agreement with the reduction of Ni sites into the brucite-like layer of LDH material. The 50 first CEPs correspond to an activation process in which (i) the increase in some irreversibly oxidized Ni(III) clusters enhances the conductivity of the Ni/Fe-LDH film and (ii) interlayered CO_3^{2-} anions of the pristine material are expulsed during the cathodic sweeps and are replaced by OH^- during the anodic sweeps. Thus OH^- anions become the predominant species into the interlayered space and further the unique exchanged anionic species during the redox process. From the 50th cycle, current, Δm and d-spacing of the electroactivated material oscillate around a stationary value *versus* the applied potential. Li^+, H_2O and OH^- are reversibly transferred with different interfacial kinetics and relative concentration changes.

At the beginning of the Ni(II) oxidation, in the range from 0.600 V to 0.650 V *vs.* SHE, the electron transfer is compensated by Li^+ desorption from the LDH external surfaces (**Eq. 14**). From 0.675 V, the gravimetric behavior suits the assumption of a switch in Ni(III)/Ni(II) redox state induces OH^- intercalation within the interlayer space, in agreement with a counterflux of water molecules (**Eq. 12**). H_2O deintercalation is opposed by the electrostatic attraction between anions and positively charged layers of the LDH. This phenomenon is responsible for the basal spacing decrease highlighted by *operando* XRD. Concomitantly, the variation of the pH at the coated interface due to OER allowes Li^+ desorption from LDH nanoplatelet external surfaces (**Eq 13**). During the cathodic sweep, Li^+ sorption onto the negatively charged external surface of the LDH nanoplatelets occurs when the OER stops. In term of mass, OH^- deintercalation is the predominant phenomenon in the potential range from the zero current density and the maximum negative Ni(III) reduction current density. When Ni(III) reduction reached its maximum, H_2O intercalation predominates. Both are responsible for the basal spacing increase highlighted by *operando* XRD as soon as the current reached zero.

Moreover the specific electrochemical properties of Ni/Fe-LDH makes it possible to control anion exchange and cation (electro)sorption capacity and thus envisage breakthrough electrolysis processes for the capture and release of ions (energy storage, water treatment, industrial effluent treatment…).

These results pave the way towards *operando* characterizations of the transfer mechanisms of species during the whole life cycle of conductive crystalline materials (LDH, graphene, MXene,...) at/in which redox processes accompanied by species (ions, solvent molecules) insertion or electro-sorption/desorption processes occur, from the transitional regime and stationary regime to the end of material life cycle. Several fields such as electrochromism, batteries, fuel cells and absorbing materials could benefit from this new approach. Finally, the simultaneous determination of the electrode mass variation, the material diffraction and the electron flow through the electrode could also allow to deeply study the electro-assisted synthesis of crystalline compounds, due to interfacial pH variation by H_2O, H^+, O_2 or NO_3^- electroreduction.

ACKNOWLEDGMENTS

The authors thank the line SIXS team for their support at synchrotron SOLEIL (Saint-Aubin, France): Dr. Alessandro Coati and Pr. Yves Garreau. They also thank Dr. Cédric Roosz for providing the schematic representation of the LDH structure and Dr. Théophile Guillon from BRGM for programming and plotting Figure 3.

Financial support was provided by the BRGM and the Labex Matisse from Sorbonne University.

AUTHOR CONTRIBUTION STATEMENT

Conceptualisation was performed by ED, SB, AS, HP and CD-C. Formal analysis was done by ED, SB, OS and CD-C. Funding acquisition was obtained by SB, II, HP and CD-C. Investigation was done by ED, SB, AS, MG, DL, AV and CD-C. Methodology was conducted by ED, SB, AS, HP, OS and CD-C. Cell design and realization were done by ED, DL and DB. Modelling was performed by ED, SB, AR, HP and OS. Writing of the original draft was done by ED, SB and CD-C. Writing, review and editing were done by ED, SB, AS,II, HP, OS and CD-C.

REFERENCES

1. C. Taviot-Guého, P. Vialat, F. Leroux, F. Razzaghi, H. Perrot, O. Sel, N. Daugaard Jensen, U. Gros Nielsen, S. Peulon, E. Elkaim and C. Mousty, *Chemistry of Materials*, 2016, **28**, 7793-7806.
2. D. L. Bish, *Bulletin De Mineralogie*, 1980, **103**, 170-175.
3. F. Cavani, F. Trifiro and A. Vaccari, *Catalysis Today*, 1991, **11**, 173-301.
4. A. Vaccari, *Catalysis Today*, 1998, **41**, 53-71.
5. M. Lal and A. T. Howe, *Journal of Solid State Chemistry*, 1981, **39**, 377-386.
6. E. Scavetta, Y. Vlamidis, T. Posati, M. Nocchetti and D. Tonelli, *Chemelectrochem*, 2016, **3**, 1320-1328.
7. L. Xu, Y. Q. Lin, X. Chen, Y. L. Lu and W. S. Yang, *Chemical Journal of Chinese Universities-Chinese*, 2016, **37**, 442-447.
8. L. Desigaux, M. Ben Belkacem, P. Richard, J. Cellier, P. Leone, L. Cario, F. Leroux, C. Taviot-Gueho and B. Pitard, *Nano Letters*, 2006, **6**, 199-204.
9. E. Duquesne, S. Betelu, C. Bazin, A. Seron, I. Ignatiadis, H. Perrot, O. Sel and C. Debiemme-Chouvy, *Journal of Physical Chemistry C*, 2020, **124**, 3037-3049.
10. E. Duquesne, S. Betelu, A. Seron, I. Ignatiadis, H. Perrot and C. Debiemme-Chouvy, *Nanomaterials*, 2020, **10**, 1832.
11. X. R. Gao, P. K. Wang, Z. H. Pan, J. P. Claverie and J. Wang, *Chemsuschem*, 2020, **13**, 1226-1254.
12. D. D. Jia, D. G. Jiang, Y. W. Zheng, H. Tan, X. Y. Cao, F. Liu, L. J. Yue, Y. Y. Sun and J. Q. Liu, *Nanoscale*, 2019, **11**, 2812-2822.
13. D. X. Guo, X. M. Song, L. C. Tan, H. Y. Ma, H. J. Pang, X. M. Wang and L. L. Zhang, *Acs Sustainable Chemistry & Engineering*, 2019, **7**, 2803-2810.
14. S. Sanati and Z. Rezvani, *Ultrasonics Sonochemistry*, 2018, **48**, 199-206.
15. Y. Wang, Z. Chen, M. Man Zhang, Y. Yaoyu Liu, H. Huixia Luo and K. Kai Yan, *Journal*, 2021, In press, Corrected proofs.
16. A. Seron and F. Delorme, *Journal of Physics and Chemistry of Solids*, 2008, **69**, 1088-1090.
17. P. Vialat, F. Leroux and C. Mousty, *Electrochimica Acta*, 2015, **158**, 113-120.
18. R. Roto and G. Villemure, *Journal of Electroanalytical Chemistry*, 2007, **601**, 112-118.
19. G. Sauerbrey, *Zeitschrift Fur Physik*, 1959, **155**, 206-222.
20. K. Bizet, C. Gabrielli and H. Perrot, *Applied Biochemistry and Biotechnology*, 2000, **89**, 139-149.
21. C. Gabrielli, J. J. Garcia-Jareno, M. Keddam, H. Perrot and F. Vicente, *Journal of Physical Chemistry B*, 2002, **106**, 3182-3191.

22. C. Gabrielli, J. J. Garcia-Jareno, M. Keddam, H. Perrot and F. Vicente, *Journal of Physical Chemistry B*, 2002, **106**, 3192-3201.
23. S. Miyata, *Clays and Clay Minerals*, 1983, **31**, 305-311.
24. T. Kameda, M. Saito and Y. Umetsu, *Materials Transactions*, 2006, **47**, 923-930.
25. S. Miyata, *Clays and Clay Minerals*, 1980, **28**, 50-56.
26. S. Miyata, *Clays and Clay Minerals*, 1975, **23**, 369-&.
27. L. O. Torres-Dorante, J. Lammel, H. Kuhlmann, T. Witzke and H. W. Olfs, *Journal of Plant Nutrition and Soil Science*, 2008, **171**, 777-784.
28. A. Di Bitetto, G. Kervern, E. Andre, P. Durand and C. Carteret, *Journal of Physical Chemistry C*, 2017, **121**, 6104-6112.
29. G. L. Gaines and H. C. Thomas, *Journal of Chemical Physics*, 1953, **21**, 714-718.
30. D. A. Corrigan and R. M. Bendert, *Journal of the Electrochemical Society*, 1989, **136**, 723-728.
31. J. B. Qiu and G. Villemure, *Journal of Electroanalytical Chemistry*, 1995, **395**, 159-166.
32. J. B. Qiu and G. Villemure, *Journal of Electroanalytical Chemistry*, 1997, **428**, 165-172.
33. F. Song and X. L. Hu, *Nature Communications*, 2014, **5**, 9.
34. P. Z. Sun, R. Z. Ma, X. Y. Bai, K. L. Wang, H. W. Zhu and T. Sasaki, *Science Advances*, 2017, **3**, 8.